Dimensional Crossover in the Superfluid-Supersolid Quantum Phase Transition

Giulio Biagioni,[1,2,*] Nicolò Antolini,[1,3,*] Aitor Alaña,[4] Michele Modugno,[4,5] Andrea Fioretti,[1]
Carlo Gabbanini,[1] Luca Tanzi,[1] and Giovanni Modugno[1,2,3,†]

[1]*CNR-INO, Sede di Pisa, 56124 Pisa, Italy*
[2]*Department of Physics and Astronomy, University of Florence, 50019 Sesto Fiorentino, Italy*
[3]*LENS, University of Florence, 50019 Sesto Fiorentino, Italy*
[4]*Department of Physics, University of the Basque Country UPV/EHU, 48080 Bilbao, Spain*
[5]*IKERBASQUE, Basque Foundation for Science, 48013 Bilbao, Spain*

Supersolids are a fundamental quantum phase of matter where the global phase and translational symmetries are spontaneously broken. The recently discovered supersolidity in quantum gases of strongly magnetic atoms gives the opportunity to explore in depth how superfluidity and crystalline order are mixed in this fascinating phase. The dipolar supersolid is usually created from a Bose-Einstein condensate, i.e., a standard superfluid, crossing a quantum phase transition that is related to the crystallization transitions of ordinary matter. In this work, we assess experimentally and theoretically the character of the superfluid-supersolid quantum phase transition. We find that one-row supersolids can have already two types of phase transitions, discontinuous and continuous, that are reminiscent of the first- and second-order transitions predicted in the thermodynamic limit in 2D and 1D, respectively. The dimensional crossover is peculiar to supersolids, is controlled via the transverse confinement and the atom number, and can be justified on the general ground of the Landau theory of phase transitions. The quasiadiabatic crossing of a continuous phase transition opens new directions of investigation for supersolids.

I. INTRODUCTION

Supersolids are a fundamental phase of matter that mixes the properties of superfluids and crystals. Proposed more than 50 years ago [1–4], a supersolid phase was recently observed in Bose-Einstein condensates of strongly magnetic atoms [5–7], featuring simultaneous breaking of the global U(1) and translational symmetries [8–10] and reduced moment of inertia under rotations [11]. The so-called dipolar supersolid requires a confinement along at least one spatial direction, so the lattice structure can develop in 1D [5–7] or in 2D [12]. The lattice is compressible, differently from that of light-induced supersolids [13,14]. The nature of the atomic interactions is such that the supersolid is of the cluster type, i.e., each lattice site hosts many atoms, of the order of 1000. This realizes the scenario first depicted by Gross [1], ensuring strong

superfluidity effects. Thanks to the tunability of the interactions, it is possible to study the quantum phase transition between the superfluid phase, a standard Bose-Einstein condensate, and the supersolid phase [5–7,15], in addition to the classical phase transition from a thermal gas to a supersolid [16].

Here we focus on the superfluid-supersolid quantum phase transition, a new fundamental phase transition whose character has been only partially assessed. In the thermodynamic limit, various models predict first-order transitions in 2D [17–19], and second-order transitions in 1D [20], in analogy to standard crystallization transitions. A transition of the latter type was observed experimentally in cavity supersolids [13,21]. For dipolar supersolids, the predicted scenario is more complex, with two types of first-order transitions for 2D lattices [22,23] and both first- and second-order transitions for 1D lattices [24,25] depending on the density. In the experiments, the problem is complicated not only by the dimensionality varying continuously between 1D and 2D but also by the finite size and the inhomogeneity due to the presence of harmonic potentials. So far, the quantum phase transition was crossed only for supersolids with 1D lattice structures. Some of the studies reported partial indications of a discontinuous [5,6,8] or a continuous transition [26], while others did not address the

*These authors contributed equally to this work.
†modugno@lens.unifi.it

character of the transition [15]. Therefore, it is not clear whether in one-row dipolar supersolids one can observe continuous, discontinuous, or both types of quantum phase transitions, nor how these transitions relate to the general theory. For trapped supersolids with 2D lattice structures, numerical simulations predict discontinuous transitions [27,28].

Although there are materials featuring density-modulated cluster phases similar to the dipolar supersolid, such as the smectic phase of liquid crystals [29] or the Rosensweig phase of ferrofluids [29,30], these phases are normally reached via classical transitions and at fixed dimensionality. Also the pair-density-wave quantum phases recently discovered in He superfluids [31,32] and in superconductors [33] have so far only been studied in 2D geometries. Hence, no results from existing phase transitions can be employed to draw predictions about dipolar supersolids.

In this work we perform a combined experimental and theoretical investigation to assess the character of the superfluid-supersolid phase transition for one-row dipolar supersolids. We find that the phase transition changes from continuous to discontinuous as the system geometry is changed from 1D to 2D, in analogy to the second-order and first-order crystallization transitions in 1D and 2D, respectively. There is, however, an important novelty due to the very nature of supersolids: the discontinuous transition can persist also for apparently 1D lattices, due to the intrinsic density background of the supersolid which keeps a 2D structure. In addition, the cluster nature of the dipolar supersolid limits the impact of finite-size effects and allows us to observe the character of the phase transition also in systems with very short lattices.

Our analysis reconciles previous results, justifies the observations on the general grounds of the Landau theory, and shows how to achieve in a controllable way continuous or discontinuous quantum phase transitions in one-row supersolids. Continuous transitions are particularly interesting as they allow us to realize excitation-free supersolids, opening new directions of investigation.

II. FORMATION OF THE DIPOLAR SUPERSOLID IN AN INFINITE SYSTEM

The geometry of the dipolar supersolids investigated experimentally is sketched in Fig. 1. The magnetic dipoles are aligned in the z direction by a magnetic field B, and an anisotropic harmonic potential is present in the three spatial directions.

To get intuition into the physics at play, we start from the infinite case, removing the confinement in the x-y plane. We consider a dipolar quantum gas at $T = 0$, described by the wave function ψ, with density $\rho = |\psi|^2$. The energy of the system is (see the Appendix B)

$$E[\psi] = E_{\text{kin}} + E_{\text{trap}} + E_{\text{cont}} + E_{\text{dd}} + E_{\text{LHY}}. \quad (1)$$
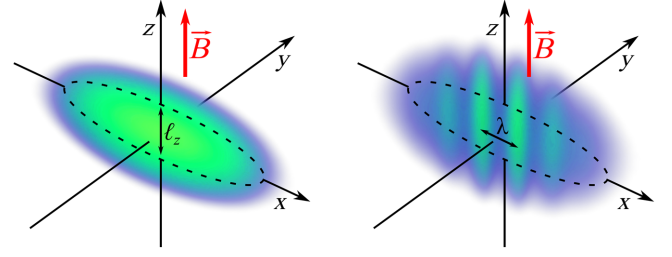

FIG. 1. Geometry of the elongated superfluid (left) and the one-row supersolid (right) commonly realized in experiments. The atomic magnetic dipoles are aligned in the z direction by the magnetic field B. The relevant length scales are the harmonic confinement length ℓ_z and the supersolid lattice spacing λ.

The first term is the kinetic energy, $E_{\text{kin}} \propto |\nabla \psi|^2$. E_{trap} describes a vertical harmonic confinement with frequency ν_z. The mean-field contact and dipolar interactions scale as $E_{\text{cont}} \propto a_s \rho^2$ and $E_{\text{dd}} \propto a_{\text{dd}} \rho^2$, where a_s is the s-wave scattering length and $a_{\text{dd}} = \mu_0 \mu^2 m / (12\pi\hbar^2)$ is the dipolar length associated with particles with magnetic dipole μ and mass m. The last term is the so-called Lee-Huang-Yang (LHY) energy, which describes the zero-point energy of quantum fluctuations in the local-density approximation [34], and scales as $E_{\text{LHY}} \propto \rho^{5/2}$.

The transition from the superfluid to the supersolid is crossed by reducing the repulsive scattering length a_s, thus increasing the relative strength of the dipolar interaction. In the supersolid phase, the dipolar energy is reduced due to the enhancement of head-to-tail arrangement of the dipoles within each cluster, but there is an increase of both contact energy, coming from an increase in the peak density, and in kinetic energy, due to the density modulation. When the dipolar gain is larger than the contact and kinetic costs, the transition takes place.

The lattice period λ of the supersolid is of the order of the harmonic length in the direction of the B field, $\ell_z = \sqrt{\hbar/2\pi m \nu_z}$, as sketched in Fig. 1, close to the wavelength of the roton excitation mode of the superfluid [35,36]. Hereinafter, we integrate out the z direction and we refer to 1D and 2D supersolids depending on the breaking of translational invariance occurring along one or two directions in the x-y plane.

At the mean-field level the supersolid is unstable, since the dipolar energy becomes more and more negative for increasing density. Collapse is eventually prevented by the repulsive LHY energy term. By further decreasing the scattering length, the system crosses a second phase transition toward a droplet crystal, where the superfluid background disappears and coherence between clusters is lost [5–7]. In the present work we do not study the latter transition.

Generally, the main features of a phase transition are captured by the Landau theory, in which the ground state of the system is determined by the behavior of the free energy

as a function of the order parameter. For crystallization phase transitions, the typical order parameter is the contrast C of the density modulation, which is zero in liquidlike phases and different from zero in crystal-like phases. Although in general C is complex, for the purpose of our analysis we can take it real; see Appendix A. The energy difference between the state with $C = 0$ and that with $C \neq 0$ can be expanded in powers of C as

$$\Delta E \simeq aC + bC^2 + cC^3 + dC^4, \qquad (2)$$

where the values of the coefficients a, b, c, d determine the character of the phase transition. In the infinite case under consideration, the linear term a is zero, but it appears when a trap is present; see Appendix A.

As usual in the context of the Landau theory, the symmetries of the ground state provide information on the character of the phase transition. Close to the transition, where $C \ll 1$, a sinusoidal modulation is a good approximation for the supersolid ground-state density [17,22,25]:

$$\rho(\mathbf{r}) = \rho_0 \left[1 + C \sum_i \cos(\mathbf{k}_i \cdot \mathbf{r}) \right], \qquad (3)$$

where ρ_0 is the average density and $\mathbf{k}_i$ the lattice wave vectors defining the lattice dimensionality.

In 1D the supersolid lattice is characterized by a single wave vector $\mathbf{k}$. In this case, ansatz (3) is symmetrical with respect to the substitution $C \rightarrow -C$, which leads only to an overall displacement of the lattice structure. Therefore, states which differ only in the sign of the contrast are physically equivalent. The free energy Eq. (2) must be an even function of C; i.e., $c_{1D} = 0$. The transition occurs when, by lowering the scattering length, the dipolar energy overcomes the contact energy and reverses the sign of the quadratic coefficient b_{1D}. Therefore, the transition is of the second order; see Fig. 2(a).

The 2D case was studied in Refs. [17,22]. The supersolid lattice is triangular, which is the closest packing configuration, with lattice wave vectors of equal length satisfying $\mathbf{k}_1 + \mathbf{k}_2 + \mathbf{k}_3 = 0$. In this case, the previous symmetry is lost, as ansatz (3) represents two very different states depending on the sign of C. For $C > 0$ it corresponds to a triangular lattice of density maxima, for $C < 0$ to a triangular lattice of holes, i.e., a honeycomb lattice. Therefore, the free-energy expansion Eq. (2) can contain odd terms, in particular the cubic term c_{2D}. This results in a discontinuous phase transition, characterized by the presence of a metastable state with finite contrast and a jump in the order parameter. In dipolar supersolids, the sign of the cubic term c_{2D} depends on the competition between kinetic and LHY energy [22]. At relatively low density, kinetic energy dominates and leads to $c_{2D} < 0$, resulting in a phase transition toward a triangular lattice with $C > 0$; see solid lines in Fig. 2(b). At high densities, the LHY contribution
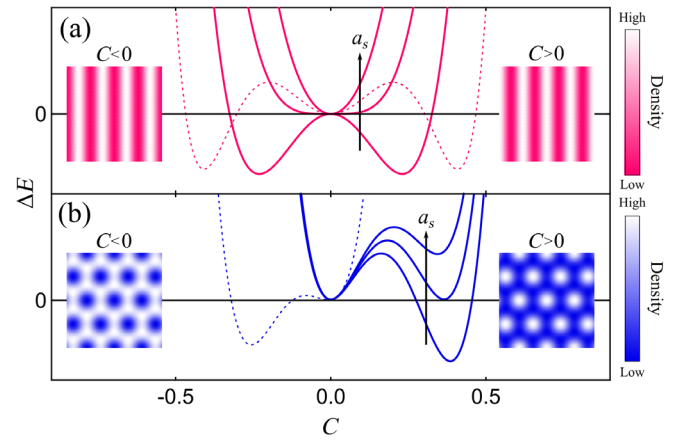

FIG. 2. Landau theory of the superfluid-supersolid quantum phase transition in the thermodynamic limit. Scenarios for second-order phase transitions in 1D (a) and first-order phase transitions in 2D (b). Solid lines are the typical behavior of the free energy as a function of the order parameter C for varying scattering length. Dashed lines are examples of the free energy in the LHY-dominated regime. Insets show the lattice structure.

becomes important and can reverse the sign of c_{2D}. In this case, the ground state is a honeycomb lattice with $C < 0$; see the dotted line of Fig. 2(b).

We note that the Landau theory allows for a discontinuous phase transition also for the 1D case, when the free energy is an even function of C. This happens if the quartic coefficient d_{1D} is negative [29]. To ensure stability, one has to expand the free energy to the sixth order. By decreasing the scattering length, one crosses a discontinuous transition as shown by the dashed line in Fig. 2(a). For the dipolar supersolid, d_{1D} is determined by the competition between kinetic energy (positive contribution) and LHY energy (negative contribution). At very high densities, therefore, when the LHY energy dominates, we expect a first-order transition also in 1D. Since the LHY term is the zero-point energy of quantum fluctuations, the discontinuous transition in this regime belongs to the class of fluctuation-induced first-order phase transitions, as those found in some types of superconductors and liquid crystals [37]. Such an effect can explain the numerical observations in Ref. [25].

III. THEORETICAL PHASE DIAGRAM IN THE TRAPPED SYSTEM IN EQUILIBRIUM

Moving to the finite-size systems studied in experiments, one should replace the thermodynamic concepts of first- and second-order phase transitions with those of discontinuous and continuous transitions. In addition, the inhomogeneity of the density in the harmonic potentials generally leads to a coexistence of the two phases.

In the supersolids realized so far, the harmonic confinement in the x-y plane is typically anisotropic, leading to the formation of one-row lattices. One would naturally

associate such configuration with the second-order phase transitions of the infinite system. However, various experiments [5,6,8] and numerical simulations [24,25] have shown the presence of apparently discontinuous transitions. To clarify the scenario, in this section we present a detailed analysis of the equilibrium states of trapped supersolids, obtained via numerical simulations.

To characterize the typical trapped systems, we fixed two of the trap frequencies to realistic values, $\nu_x = 20$ Hz and $\nu_z = 80$ Hz, which result in a supersolid elongated in the x direction. We then varied both the transverse frequency ν_y and the atom number N in realistic ranges, and for each set of values we studied the evolution of the ground state of the system as a function of the scattering length a_s. The ground state was obtained by minimizing numerically the energy in Eq. (1), with the addition of trap energies also in the x and y directions.

Figure 3 presents a summary of the simulations. Figure 3(a) shows the presence of various regions of continuous and discontinuous transitions in the $N - \nu_y$
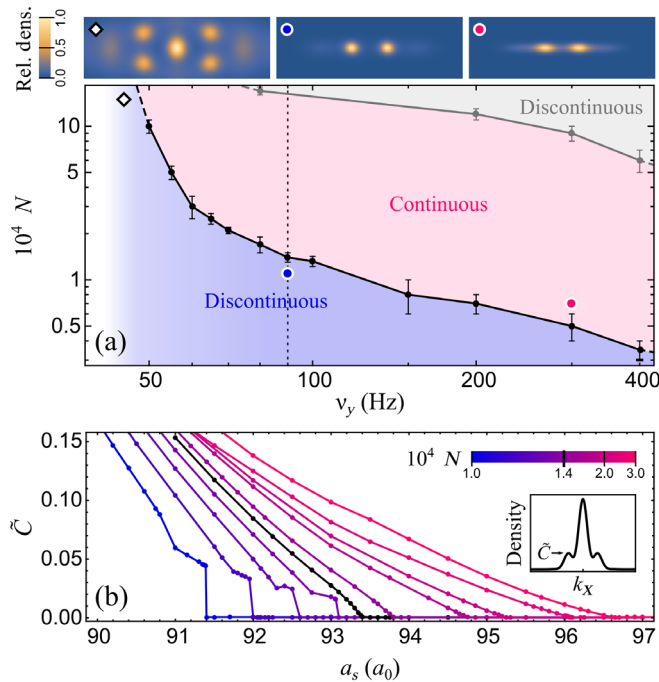

FIG. 3. Character of the superfluid-supersolid phase transition from numerical simulations. (a) Character of the transition as a function of the atom number N and the trap frequency ν_y. Black dots mark the boundary between the continuous and discontinuous regimes. Error bars are the atom number resolution in the simulations. Gray dots mark the onset of the LHY-dominated regime. Insets: samples of supersolid density distributions. From left to right, peak densities are 5.48×10^{11}, 3.19×10^{11}, and 1.98×10^{11} cm^{-2}. (b) Contrast as a function of the scattering length for different values of N, and $\nu_y = 90$ Hz [dashed line in (a)]. The curve corresponding to the continuous-discontinuous boundary is plotted in black. Solid lines are a guide for the eye. Inset: definition of the contrast in momentum space.

plane. For small ν_y, the trap approaches a circular shape in the x-y plane and the supersolid forms on two rows with a triangular structure. There, we find a discontinuous transition, in analogy with the first-order phase transition in 2D discussed in Sec. II. By increasing the transverse frequency, at first we continue to observe discontinuous transitions although the supersolid apparently forms on a single row, and only for large frequency we observe continuous transitions as expected for 1D systems. For large N, Fig. 3(a) shows a second regime of discontinuous transitions, which we discuss later. The regime of small N is instead irrelevant, since the supersolid lattice shrinks to a single cluster.

The specific order parameter we consider is the contrast in momentum space $\tilde{C}$, i.e., the height of the Fourier peak at $k = 2\pi/\lambda$, related to the real-space contrast by $\tilde{C}^2 = C^2/16$, in the limit of small C (see Appendix B). As we show in the next section, this choice is motivated by the presence of a related experimental observable. Figure 3(b) shows examples of the phase transitions for fixed $\nu_y = 90$ Hz and variable N. While for large atom numbers $\tilde{C}$ changes smoothly with a_s, for smaller N the transition is discontinuous, with a finite jump in the contrast. We arbitrarily chose the boundary between continuous and discontinuous transitions as the smallest value of N that gives a jump in $\tilde{C}$ at the transition point smaller than 0.001. Such a boundary can be thought of as a line of tricritical points [38].

Note that all transitions we explored numerically end up in distributions with moderate or large density overlap between neighboring clusters, a necessary condition for preserving the global phase coherence typical of supersolids [4]. As shown by the sample distributions in Fig 3(a), the supersolid lattice forms in the central region of the system, while the low-density sides tend to remain in the superfluid regime. However, their weight is normally very small, so the behavior of the system is dominated by the supersolid.

Although in most of the phase diagram the supersolid seems to develop with a single row of maxima, a Fourier analysis reveals the presence of a triangular structure of the density background. An example of such analysis is shown in Fig. 4. One notes the presence of Fourier peaks not only along the x direction but also along the y direction, although with much smaller amplitude and larger momentum; see Figs. 4(c) and 4(d). Therefore, even in the presence of a single row of principal density maxima there is clearly a persistence of the triangular structure of the 2D supersolid. Both amplitude and momentum change continuously when moving along the dimensional crossover; see Figs. 4(e) and 4(f). Interpreting the changing character of the transition in terms of the Landau theory, we conclude that the main effect of an increasing atom number is to suppress progressively the 2D triangular structure. This results in a progressive suppression of the cubic terms in the
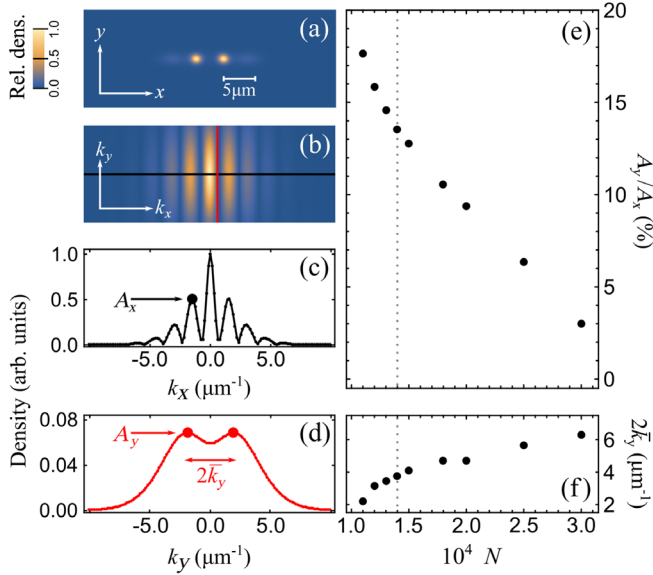
FIG. 4. Two-dimensional structure of the density background across the dimensional crossover. Real-space (a) and Fourier-space (b) simulated density of a supersolid with $N = 1.4 \times 10^4$ and $\nu_y = 90$ Hz, at the continuous-discontinuous boundary. Peak density in (a) is 2.14×10^{11} cm^{-2}. (c),(d) Cuts in the Fourier space, along the black line (c) and the red line (d) in (b) reveal the presence of peaks in both x and y directions. (e) Ratio of the Fourier amplitudes along y and x, and (f) Fourier spacing along y, for the simulations of Fig. 3(b), at $\tilde{C} \simeq 0.04$. Vertical dotted lines mark the continuous-discontinuous boundary.

energy expansion, especially the kinetic energy term, which weakens the discontinuity until the transition becomes continuous. There is a similar effect increasing ν_y at constant N.

The prevalence of discontinuous transitions in the $N - \nu_y$ plane of Fig. 3(a) is due to a change of the compressibility of the supersolid for varying atom numbers. At small N, the clusters are more compressible and the triangular structure can be deformed more easily by the transverse confinement. This favors discontinuous transitions over continuous ones. Additional analysis of the simulated density distributions shows that the transverse size σ_y of the supersolid at the phase transition at the continuous-discontinuous boundary is very close to the harmonic oscillator length ℓ_y, i.e., the size of a noninteracting system; see Appendix B 2. This supports the idea that the transition becomes discontinuous when there is enough space in the trap to accommodate a 2D structure.

In the phase diagram of Fig. 3(a) we observe also two clear effects of the LHY energy term in Eq. (1), which is normally small until one reaches the regime of large densities, i.e., large N. The first effect is the presence of the additional continuous-discontinuous boundary for large N. This is due to a gradual increase of the LHY energy as the supersolid contrast increases, since the density also increases. The LHY contribution reverses the sign of the

quartic term in the Landau expansion and changes the transition from continuous to discontinuous, as discussed in Sec. II. It is therefore a fluctuation-induced phase transition, related to the one found in the infinite case of Ref. [25]. The second effect is a gradual elongation along y of the clusters for increasing N and decreasing ν_y. This effect is due to the increasing cost in LHY energy, which favors the formation of a 1D lattice of "stripes" directed along y instead of a triangular lattice, as observed in previous simulations [23,39]. This effect broadens the region of continuous phase transitions in the upper left part of the $N - \nu_y$ plane. See Appendix B for further discussion.

Finally, in the simulations we observe a small modulation appearing in discontinuous transitions just before the jump to higher contrast states, resulting in a mixing of continuous and discontinuous transitions. In the framework of the Landau model, we interpret such an effect as a consequence of the trapping energy, which introduces a term linear in C in the energy expansion (see Appendix A). This term is responsible for a small asymmetry between C and $-C$, which tends to produce a weak modulation of the density even on the superfluid side. This effect was seen previously in numerical simulations of dipolar Bose-Einstein condensates [40].

IV. EXPERIMENTAL EVIDENCE OF CONTINUOUS AND DISCONTINUOUS PHASE TRANSITIONS

We tested experimentally the theoretical predictions on a supersolid made of ^{162}Dy magnetic atoms with dipolar length $a_{dd} = 130a_0$, trapped in optical potentials. To move from continuous to discontinuous transitions it is sufficient to change the aspect ratio of the harmonic potential in the y-z plane, at constant atom number. We chose in particular two potentials featuring continuous or discontinuous transitions. Potential V_C, with frequencies $(\nu_x, \nu_y, \nu_z) = [15.0(0.7), 101.0(0.3), 93.9(0.6)]$ Hz, provides a strong confinement along y, leading to a continuous transition. Potential V_D, with frequencies $[21.8(1.0), 67.0(0.8), 102.0(0.7)]$ Hz, provides instead a weaker confinement along y, leading to a discontinuous transition. Figure 5 shows the predicted evolution of the contrast $\tilde{C}$ with the scattering length from the ground-state simulations. In both cases, the mean atom number at the transition is about $N = 3 \times 10^4$. Both configurations correspond to one-row supersolids.

Unlike the theory presented so far, in the experiment we study the dynamical evolution of the system for varying a_s, starting from the superfluid side of the transition. This does not necessarily correspond to following the equilibrium ground state. The dynamical nature of the problem involves concepts not discussed so far, such as adiabaticity, dissipation, and, in the case of discontinuous phase transitions, hysteresis.
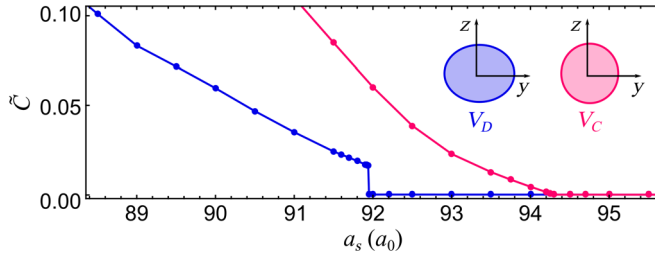
FIG. 5. Equilibrium transitions in the experimental configurations. Simulated momentum-space contrast versus scattering length for harmonic potentials V_D (blue) and V_C (magenta) with $N = 3 \times 10^4$. Inset: shape of the contour lines in the y-z plane for the two potentials.

The experiments start from a standard superfluid, at typical temperatures $T \leq 10$ nK. The scattering length is then slowly reduced by means of a magnetic Feshbach resonance. The speed of the magnetic-field ramp was chosen as a compromise between adiabaticity and a not too large impact of the unavoidable three-body losses [5]. The optimal ramp speed, $\dot{a}_s = 0.5a_0/\text{ms}$, allows us to ramp across the transition in potential V_C almost adiabatically. We note that the three-body loss rate scales as ρ^2, so it reaches its maximum value at the density peaks in the supersolid phase. These losses have both a detrimental and a beneficial effects for the study of the phase transition. If on the one hand they decrease ρ over time, on the other hand they introduce a moderate damping of the excitations connected to a local increase in density (see Appendix C 4 for details).

We studied the system via absorption imaging after a sudden release from the optical potential, followed by a long free expansion. Just before the release, we rapidly increase the scattering length to a large value ($a_s \simeq 140a_0$) in order to reduce the relative effect of the dipole-dipole interaction (see Appendix C 1) [6]. The measured distribution, see examples in Fig. 6(a), can be related to the theoretical momentum distribution, $\rho(k_x, k_y)$, although there are small modifications due to interactions during the expansion. The main observable is the contrast $\tilde{C}$, i.e., the relative height of the peak at the characteristic momentum of the supersolid, as in the theory (see Appendix C 2).

Figure 6 presents the main experimental observations when crossing the superfluid-supersolid transition in potentials V_C and V_D. In particular, we study the evolution of $\tilde{C}$ for an ingoing ramp from the superfluid to the supersolid (filled circles) and for a subsequent outgoing ramp from the supersolid to the superfluid (open circles). The experimental trajectories in the $a_s - t$ plane are shown in Fig. 6(a). The holding time before imaging is 20 ms, which we found to be sufficient to form the supersolid.

Phase transitions in potentials V_C and V_D show completely different behaviors; see Figs. 6(b) and 6(c). In potential V_C [Fig. 6(b)], the ingoing ramp shows a smooth
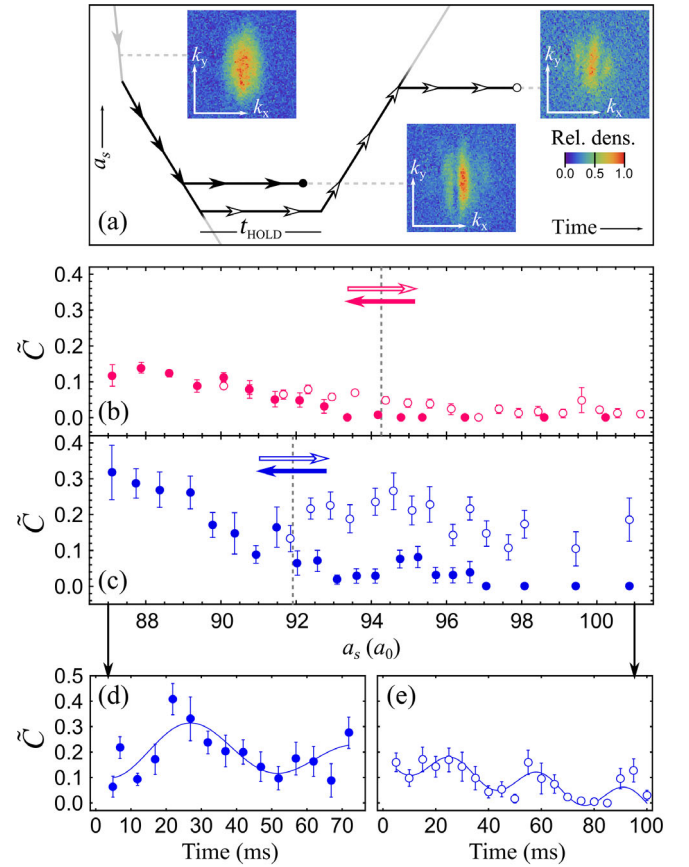

FIG. 6. Experimental observation of continuous and discontinuous phase transitions. (a) Trajectories in the $a_s - t$ plane for the ingoing (filled symbols) and outgoing (empty symbols) ramps. Insets: examples of experimental momentum distributions, from left to right, in the superfluid, supersolid, and excited superfluid regimes for potential V_D. (b),(c) Contrast $\tilde{C}$ versus scattering length during ingoing (dots) and outgoing (circles) ramps for potentials V_C (b) and V_D (c), respectively. Vertical dashed lines mark the theoretical position of the transitions. (d), (e) Time evolution of $\tilde{C}$ for potential V_D at $a_s = 87.3a_0$ in the ingoing ramp (d) and at $a_s = 100.3a_0$ in the outgoing ramp (e), respectively. Dots are experimental data, lines are fits with a damped oscillation model. Error bars represent the standard error of the mean of about 10–20 measurements.

increase of $\tilde{C}$, with small shot-to-shot fluctuations. During the outgoing ramp $\tilde{C}$ returns gradually to zero, indicating that the phase transition can be crossed sequentially in the two directions without creating large excitations.

In potential V_D instead [Fig. 6(c)], the ingoing ramp shows strong fluctuations of $\tilde{C}$ already before the phase transition, in the region $(97–93)a_0$, followed by a steep increase of $\tilde{C}$ around $93a_0$. At the transition we also observe a jump in the atom number due to the increase of density in the supersolid phase; see Appendix C 4. Remarkably, during the outgoing ramp, $\tilde{C}$ remains very large, for up to at least $10a_0$ in the superfluid regime. While transition V_C can be crossed back and forth almost

adiabatically for our ramp speed, crossing transition V_D is manifestly nonadiabatic. The two behaviors are consistent with continuous and discontinuous phase transitions, respectively. We checked that the difference in adiabaticity for the two transitions persists for the whole range of ramp speeds that can be achieved experimentally; see Appendix C 6.

In potential V_D, we observe strong excitations of various collective modes by crossing the transition. In particular, we focus on the oscillation of the order parameter $\tilde{C}$. Figures 6(d) and 6(e) show the dynamics of $\tilde{C}$ for two selected values of a_s after the ingoing and outgoing ramps. After the ingoing ramp [Fig. 6(d)], the oscillation amplitude is smaller than its mean value, so a finite contrast persists throughout the observed time evolution. The oscillation frequency, $\nu = 21(3)$ Hz, is consistent with the so-called amplitude mode of the supersolid, already studied in Ref. [8]. After crossing back the transition [Fig. 6(e)], we still observe a sinusoidal oscillation. However, in this case the oscillation's amplitude is comparable with its mean value, so $\tilde{C}$ is about zero in its minima. Since $\tilde{C}$ is proportional to the square of the real-space contrast C, we identify such oscillation with an excited mode of the superfluid with zero mean value of C. Such oscillations are also present for potential V_C but with much smaller amplitude, so we can associate them to a nonadiabatic crossing of the phase transition from the supersolid to the superfluid. Note that the experimental $\tilde{C}$ for potential V_D in the static measurements of Fig. 6(c) is larger than the simulated one (Fig. 5) due precisely to the presence of such excited mode of the superfluid, since the measurements are performed close to the first maximum of the oscillation.

To corroborate theoretically these observations, we performed numerical simulations of the dynamics of a simplified zero-temperature system, without quantum fluctuations (besides the LHY energy term), and without losses. Although this system is different from the real one because it lacks dissipation, it allows us to confirm the nature of the observations without introducing phenomenological parameters like temperature or loss rate. Because of the absence of dissipation, the simulations employ scattering-length ramps slower by one order of magnitude than in the experiment, $\dot{a}_s = 0.05a_0/\text{ms}$, to achieve a quasiadiabatic crossing of the continuous transition. See Appendix D for details.

The simulations confirm the different nature of the observed oscillations. As shown in Fig. 7, the ingoing ramp excites the amplitude mode of the supersolid, with $\tilde{C}$ featuring small-amplitude oscillations around a relatively large value. The outgoing ramp produces instead an oscillation of $\tilde{C}$ with smaller amplitude and with minima at zero, corresponding to an oscillation of the real space C around zero, as shown by the samples of the real-space densities in Figs. 7(f)–7(h). Additional simulations show that the latter oscillation can be excited also at fixed
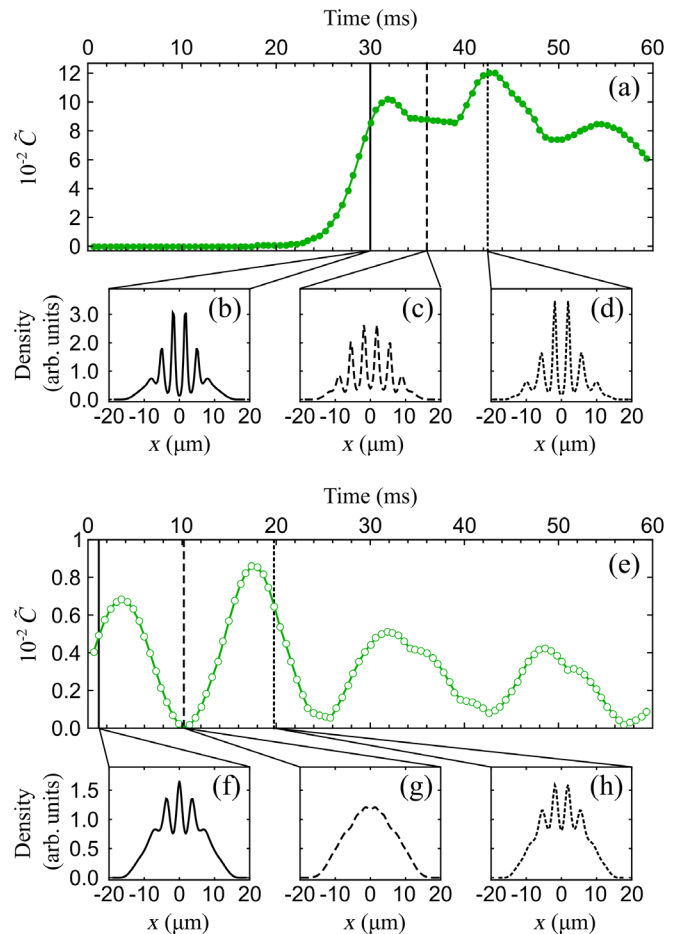

FIG. 7. Numerical simulations of the dynamics. Contrast for potential V_C as a function of time, following an ingoing ramp from $95a_0$ to $93a_0$ (a) or an outgoing ramp from $90a_0$ to $95a_0$ (e). Panels (b)–(d) and (f)–(h) show examples of the density distribution along x at specific times [vertical lines in (a) and (e), respectively].

scattering length on the superfluid side of the transition, by imposing an initial density modulation similar to that of the supersolid. Furthermore, the oscillation amplitude becomes very small if one removes the dipolar energy term from Eq. (1). This indicates that the oscillations are an excited mode of the superfluid, related to the so-called roton mode [41], but in a regime of large amplitudes.

In the experiment, crossing the phase transition produces other types of excitations besides the specific amplitude mode analyzed so far, with amplitudes systematically larger in potential V_D than in potential V_C. In particular. we observe the so-called lattice mode of the supersolid [5], as well as additional longitudinal and transverse modes. In order to quantify the different degree of excitation for the two potentials, we measured the total energy in the momentum distribution after the free expansion, $E_{\text{exp}} = \hbar^2 \langle k_x^2 + k_y^2 \rangle / (2m)$. This quantity overestimates the total energy of the system immediately after the removal of the potential, due to the subsequent increase
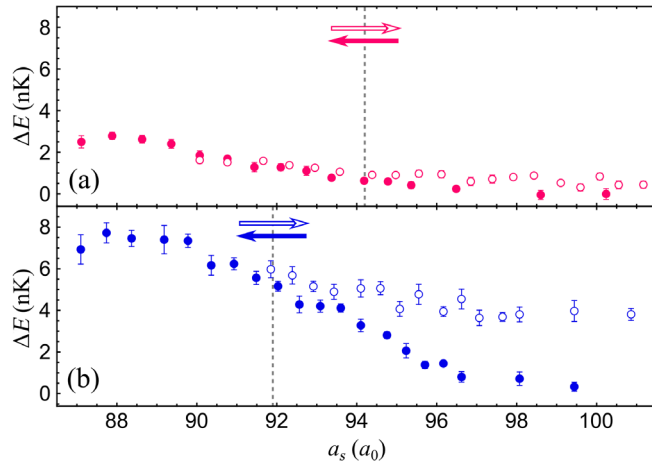
FIG. 8. Experimental energy variation across the phase transitions. Variation of the expansion energy for potential V_C (a) and potential V_D (b), during the ingoing (filled circles) and outgoing (empty circles) ramps. Error bars are the standard error of the mean of 10–20 measurements.

of a_s during the first phase of the expansion. Figure 8 shows the variation ΔE of the expansion energy with respect to the superfluid with the largest a_s. The stronger excitation for potential V_D for both ingoing and outgoing ramps is apparent. A quantitative comparison of the two ingoing ramps is difficult, since the supersolid in potential V_D has generally a larger contrast, which implies larger E_{exp}. A comparison can instead be made for the outgoing ramps, since both end in the superfluid regime. Here, potential V_D shows an excess energy $\Delta E \simeq 4$ nK, much larger than in potential V_C, $\Delta E \simeq 0.5$ nK. This is a further evidence of the different character of the phase transitions in the two potentials. The numerical simulations show a difference in excess energy when crossing the two phase transitions of the same order of magnitude, $\Delta E \simeq 0.2$ nK for potential V_C and $\Delta E \simeq 1$ nK for potential V_D; see Appendix D for details.

We verified that the phase transitions in the experiment lead from the superfluid to a coherent supersolid, by checking that the fluctuations of the phase of $\rho(k_x)$ are small [5]. This happens in the whole scattering length regions below the transitions in Figs. 6(d) and 6(e). Interestingly, the variance of the phase for potential V_C is much smaller than that for V_D, implying that also phase excitations are minimized by crossing the continuous phase transition. See Appendix C 3 for details.

A relevant question is whether the discontinuous transition in potential V_D shows hysteresis similarly to first-order phase transitions, i.e., different locations of the phase transition depending on the direction in which the transition is crossed. However, the concept of hysteresis (in the thermodynamic sense) applies only to systems that are in equilibrium. Our system is out of equilibrium, as it cannot entirely dissipate the energy acquired when crossing the

transition from the superfluid to the supersolid. Therefore, we do not expect to observe hysteresis. In the dynamical measurements as in Figs. 6(d) and 6(e) we indeed do not observe any hysteresis, within our current resolution of $2a_0$. The simulations predict a hysteresis of just about $0.5a_0$ in the hypothetical equilibrium case; see Appendix D.

V. EXPERIMENTAL FLUCTUATION SPECTRUM

A confirmation of the different character of the two phase transitions comes from an analysis of the fluctuations of the contrast. Fluctuations are generally enhanced in the vicinity of a phase transition, including the superfluid-supersolid phase transition [15]. We already noted the presence of shot-to-shot fluctuations of $\tilde{C}$ for the data in Figs. 6(a) and 6(b). These fluctuations can have quantum, thermal, or technical origin, the latter being presumably dominated by the shot-to-shot fluctuations in the atom number, which in turn determine fluctuations in the critical scattering length. One expects the fluctuations to have different distributions for continuous and discontinuous phase transitions, due to the different shape of the Landau free energy (see, e.g., Ref. [42]).

Figure 9 presents the distributions of $\tilde{C}$ measured for the two transitions, binned in four intervals of scattering length: well before, just before, just after, and well after the transition. For potential V_C, the distributions show the expected behavior of a continuous phase transition; see Fig. 9(a). For large a_s (region I), the system is in the superfluid phase in each experimental run. For smaller a_s, when the modulation appears (region II), a portion of the samples comes apart from the peak at zero contrast, populating a region of small contrasts nearby. Deeper into the supersolid region (region III), the peak at zero contrast is depleted and the system occupies a well-defined set of contrasts. Decreasing further a_s toward the droplet crystal regime (region IV), the contrast becomes larger on average but also noisier, probably because of the enhancement of three-body losses which modify from shot to shot the density distribution, depending on the details of the dynamical formation process.

For potential V_D, see Fig. 9(b), the situation is quite different. Just before the transition (region II), the histogram separates into two peaks: a main one at zero contrast and a smaller one at finite contrast. We interpret the latter peak as due to fluctuations into the second minimum of the Landau free energy, across the barrier. Moving toward the droplet crystal, the double-peak structure changes to the same broad distribution of the continuous case.

The experimental observations are corroborated by the Landau free energy calculated from realistic models of the trapped supersolids in potentials V_C and V_D, shown in Figs. 9(c) and 9(d). While the continuous transition in potential V_C has a single minimum, the discontinuous transition in V_D has two minima, which in the experiment can be populated alternatively depending on thermal,
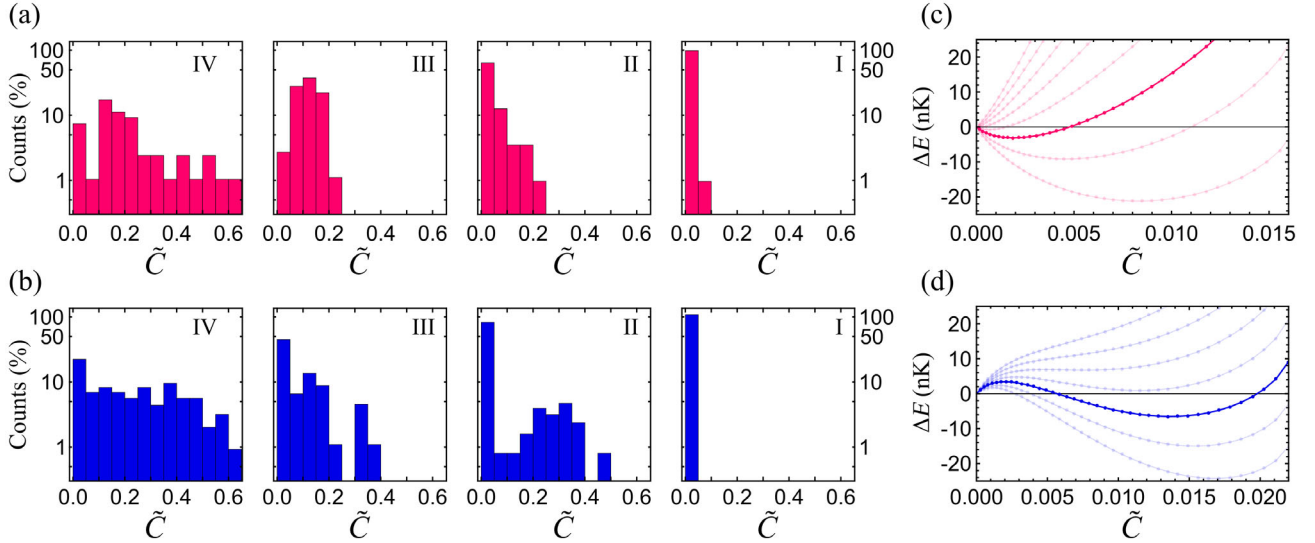
FIG. 9.   Character of the phase transition from fluctuation spectra. (a),(b) Histograms of the contrast fluctuations for potential V_C (a) and for potential V_D (b). Panels correspond to the following scattering length intervals (in units of a_0). V_C: 101–96.5 (I), 96.5–92.5 (II), 92.5–89.8 (III), 89.8–86 (IV). V_D: 101–96.7 (I), 96.7–92.3 (II), 92.3–90.3 (III), 90.3–86 (IV). Each region contains 100–150 samples. (c),(d) Theoretical model of the Landau free energy for V_C (c) and V_D (d), for scattering lengths spaced by $1.0a_0$ and $0.25a_0$ around the central values $94a_0$ and $90a_0$, respectively. Single- and double-peak structures in the experimental data in region II for V_C and V_D are in qualitative agreement with the theoretical model close to the transition, dark lines in (c) and (d).

quantum, and technical fluctuations [42]. The model is not exact, as it describes the transition with the variation of a single parameter, the contrast $\tilde{C}$, while from the numerical simulations we observe a global change of the wave function. See Appendix A 3 for details and further discussions. However, there is a qualitative agreement between the experiment and the model, in terms of both the characteristic contrast at the discontinuous transition and the characteristic energy gained by crossing the discontinuous transition. The height of the barrier at the transition in Fig. 9(d) is indeed about 5 nK, which is of the same order of both the energy gain in Fig. 8 and the system temperature.

In conclusion, the different shape of the fluctuation spectra of the contrast provides an additional evidence of the different character of the two phase transitions, continuous for potential V_C and discontinuous for V_D.

VI. DISCUSSION AND CONCLUSIONS

In summary, we assessed the character of the superfluid-supersolid quantum phase transition. By tuning the system parameters, we observed a gradual change from 1D-like configurations with continuous phase transitions into 2D-like configurations with discontinuous phase transitions. The dimensional crossover is due to the very nature of the supersolid. Although our supersolids have only a single row of principal density maxima, they keep a 2D structure thanks to the presence of the background density associated to their superfluid nature. The 2D structure is gradually suppressed by an increasing transverse

confinement or an increasing atom number. Our analysis establishes also a link between previous numerical simulations for infinite systems, showing that the discontinuous transition seen in quasi-1D at low density [25] has the same nature of the discontinuous transition in 2D [22].

The continuous-discontinuous character of the transition is controlled experimentally by changing the transverse confinement. We achieve various evidences of the different character of the transition in the two regimes, in particular from the striking difference in the adiabaticity with which the phase transition can be crossed, besides the different shape of the fluctuation spectrum. The continuous transition can be crossed almost adiabatically despite the limited timescales of the experiment, with a residual energy increase of just about 0.5 nK. The discontinuous transition is quite sharp despite the very small length of the supersolid lattice, which has only 2–3 sites. That supports the expectation that broadening effects are determined by the number of particles ($N \simeq 10^4$ here) and not by the number of sites [43].

Our findings have implications for future studies of the supersolid phase of matter. Crossing continuous quantum phase transitions we achieve supersolids that are almost free of excitations. This is an important prerequisite to study a key property of supersolids, the reduced superfluidity due to the crystal-like structure [4]. Our results can be extended directly to annular configurations, which are the ideal setup to study superfluidity [4,24,44] and would also allow us to eliminate the longitudinal harmonic potential without the edge effects introduced by boxlike potentials [45]. A sufficiently tight radial confinement will

allow us to achieve continuous phase transitions, in analogy with the 1D-like configurations we explored in this work. The control of continuous quantum phase transitions opens up also the possibility to study the generation of entanglement in the supersolid phase. Indeed, the increase of correlations in a quantum transition can lead to the creation of many-body entanglement [46]. Crossing adiabatically a continuous transition would limit the impact of noise and decoherence which usually leads to degradation of fragile entangled states. Understanding quantum correlations in the supersolid would be an important step both for developing a full quantum description of this new phase of matter and for the possible exploitation of metrologically useful entangled states [47].

APPENDIX A: LANDAU MODEL FOR THE DIPOLAR SUPERSOLID

In this Appendix, we discuss in more detail the super-fluid-supersolid phase transition in the framework of the Landau theory. Generally, for crystallization transitions the order parameter is complex: $C = |C|e^{i\phi}$, where ϕ determines the phase of the supersolid lattice. In infinite systems there is no energy cost in changing ϕ, see, for example, the case of lattice supersolids [13,21], which corresponds to the appearance of a zero-energy Goldstone mode, a signature of continuous symmetry breaking [38]. In that case, one can neglect the phase dependence of the free energy and take C to be real. In the presence of a trap, the energy depends also on ϕ and one should build a Landau model with a complex order parameter. For dipolar supersolids, however, it was shown that the associated Goldstone mode has a much lower energy than the amplitude mode [9]. This allows us again to neglect the phase and consider C real, as we do in this work.

1. 1D system

First, we consider the case of a 1D density modulation of the form $\rho(x) = \rho_0[1 + C\cos(kx)]$ that provides a good characterization of the one-row configuration. Inserting this ansatz into the energy functional Eq. (1) and expanding in powers of C leads to a Landau expansion of the form of Eq. (2), where the coefficients depend on the wave vector k, the mean density ρ_0, and the scattering length a_s. The

odd terms are exactly vanishing, as a consequence of the symmetry in the sign of the contrast discussed in the main text. Both contact and dipolar energies contribute only to the quadratic coefficient b_{1D}, since they are quadratic in the density. The coefficient b_{1D} decreases as the scattering length is decreased, and becomes negative when the attractive part of the dipolar interaction dominates, favoring the formation of the supersolid state. The other coefficients are determined only by the kinetic and LHY energy, which are a more complicated function of the density. The fourth- and the sixth-order coefficients d_{1D} and e_{1D} read

$$d_{1D} = \frac{\hbar^2\pi}{32m}|k|\rho_0 - \frac{15\pi g_{LHY}}{512|k|}\rho_0^{5/2},$$

$$e_{1D} = \frac{\hbar^2\pi}{64m}|k|\rho_0 - \frac{25\pi g_{LHY}}{8192|k|}\rho_0^{5/2}, \qquad (A1)$$

where the coefficient of the LHY energy g_{LHY} is defined after Eq. (B 1). In the experimental density regimes, the contribution of the kinetic energy (first term on the right-hand sides) dominates over that of the LHY (second term). The coefficient d_{1D} is then positive and the next-order term of the form $e_{1D}C^6$ does not change the scenario of a continuous phase transition. When instead the density is large enough, quantum fluctuations overcome the kinetic energy reversing the sign of d_{1D}. To ensure stability of the system, one has to consider the term $e_{1D}C^6$. The resulting Landau energy $\Delta E = b_{1D}C^2 + d_{1D}C^4 + e_{1D}C^6$ predicts a discontinuous phase transition with the combination $b_{1D} > 0, d_{1D} < 0, e_{1D} > 0$. The shape of the energy is depicted in Fig. 2(b). This mechanism justifies the discontinuous phase transitions at high densities and high trap frequencies depicted in gray in Fig. 3.

The previous simple model can be extended to include the effects of the trap. We modify the density ansatz into $\rho(x) = \rho_0 g(x)[1 + C\cos(kx)]$, where $g(x)$ is a Gaussian envelope of width σ which contains the proper normalization constant. As a result of the presence of the envelope, the symmetry in the sign of the contrast is broken. The two density distributions with C and $-C$ are indeed slightly different, since they have the main maximum and the central minimum at the center of the trap, respectively. Consequently, odd terms appear in the Landau energy. We have checked that odd terms are below 10% of the even terms in the relevant regime in which more than one cluster is present, and approach zero when many clusters are present, i.e., when $k\sigma$ is large. The presence of the trap introduces also linear terms in the contrast. In particular, the trap energy is proportional to the density, so it contributes only to the linear term. The interpretation of this fact is clear: a state with $C > 0$ is favorable in trap energy compared to a superfluid with $C = 0$, since it increases the density in the center of the trap and forms lateral minima where the trap potential is higher. The presence of a trap-induced linear term in the Landau energy can

explain the mixing of continuous and discontinuous phase transitions observed in the simulations. Indeed, in configurations where the transition is discontinuous, the presence of a linear term can induce a continuous transition toward states of small contrast, followed by a jump toward the second minimum at higher contrast.

2. 2D system

In the 2D infinite case, the full calculation of the Landau energy with a sinusoidal ansatz of the form Eq. (3) was reported in Ref. [22]. We checked to what extent this model applies to our case with a harmonic potential in the y direction, modifying the ansatz into $\rho(x, y) = \rho_{2D}(x, y)g(y)$, where ρ_{2D} is given by Eq. (3) and $g(y)$ is a Gaussian envelope in the transverse y direction of width σ. The expansion coefficients are equal to the thermodynamic limit in 2D until $\sigma k/(2\pi)$ approaches 0.4, a regime in which the first lateral rows of clusters are already suppressed to approximately 10%. That is not dissimilar from the results of the numerical simulations in Fig. 4, which show the change to continuous transitions when the lateral rows are suppressed to a similar level.

3. Landau model for the experimental configurations

To estimate the Landau free energy for the experimental configurations, we developed a specific model. To take into account the effect of the trap confinement, we modify ansatz (3) into

$$\rho(\mathbf{r}) = A\left[1 + Ce^{-x^2/2w_x^2}\sum_i \cos(\mathbf{k}_i \cdot \mathbf{r}')\right]$$
$$\times (1 - x^2/R_x^2)e^{-y^2/2\sigma_y^2}(1 - z^2/R_z^2), \quad \text{(A2)}$$

where we add a Gaussian envelope of width σ_y in the y direction and a Thomas-Fermi envelope of radius R_x (R_z) in the x (z) direction. The lattice vectors are $\mathbf{k_1} = 2\pi/\lambda(0, 1, 0)$, $\mathbf{k_2} = -2\pi/\lambda(\sqrt{3}/2, 1/2, 0)$, $\mathbf{k_3} = 2\pi/\lambda(\sqrt{3}/2, -1/2, 0)$, $\sqrt{3}\lambda$ is the lattice period, C is the contrast, $\mathbf{r}' = (x - \sqrt{3}\lambda, y, 0)$, and A is a normalization constant. We also add a Gaussian envelope for the sinusoidal modulation with width w_z to get a better agreement with the simulated density distributions; see Fig. 10.

To calculate the free energy as a function of C, we integrate numerically the energy functional Eq. (1) with ansatz (A2). We set all the other parameters to realistic values obtained from the numerical simulations of the ground state, $R_x = 8.1\ell_x$ ($R_x = 5.6\ell_x$), $\sigma_y = 0.64\ell_y$ ($\sigma_y = 0.46\ell_y$), $R_z = 4.9\ell_z$ ($R_z = 5.1\ell_z$), $w_x = 2.1\ell_x$ ($w_x = 1.9\ell_x$), $\lambda = 1.6\ell_x$ ($\lambda = 1.9\ell_x$) for trap V_C (V_D). This approximation allows us to study the free energy as a function of the order parameter only. For a better comparison with the experimental and numerical data, we
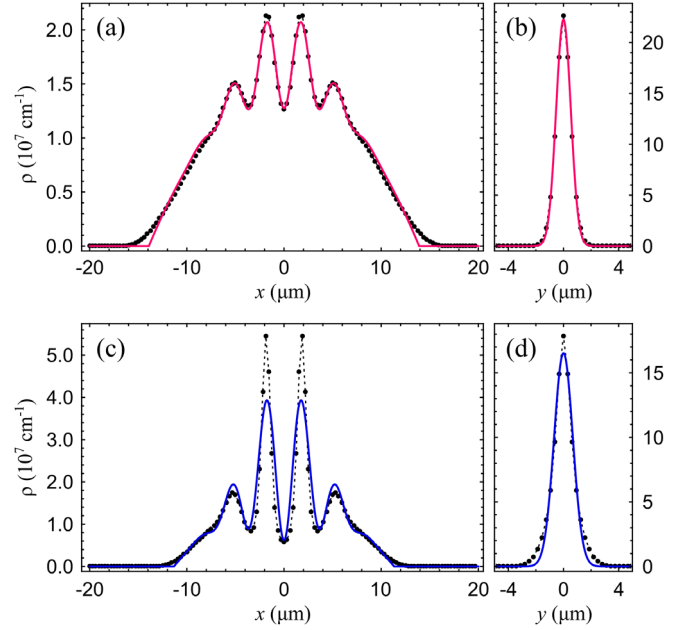

FIG. 10. Comparison between the ground-state simulations and ansatz (A2). (a),(b) Black points are the integrated density along x (a) and y (b) directions for potential V_C. Solid lines are 1D cuts of ansatz (A2) fitted to the simulated densities. (c),(d) Same for potential V_D. Simulations correspond to supersolid states just after the transition ($94.25a_0$ for V_C and $91.94a_0$ for V_D).

express the energy as a function of $\tilde{C}$, calculated from the Fourier transform of the wave function.

The results for the two experimental potentials V_C and V_D are plotted in Fig. 9 for various values of the scattering length across the phase transitions. As discussed in Sec. III, $\tilde{C}$ scales as C^2, so the shape of the free-energy curves is somewhat different from those in Fig. 2. The model correctly reproduces the character of the transition for the two potentials: while for potential V_C the minimum of the energy smoothly increases from $\tilde{C} = 0$ to $\tilde{C} > 0$, for potential V_D a second minimum develops by lowering the scattering length, resulting in a finite jump of $\tilde{C}$ at the transition. For potential V_C, the critical scattering length is around $96a_0$, slightly above the numerical value of $94a_0$. For potential V_D the transition is at $90a_0$ instead of $91.9a_0$. For both V_C and V_D the value of the contrast at the transition is of the same order of that calculated in the numerical simulations (see Fig. 5).

APPENDIX B: NUMERICAL SIMULATIONS OF THE PHASE TRANSITION IN EQUILIBRIUM

1. Numerical methods

In this Appendix, we present the methodology followed for the numerical simulations of the equilibrium phase diagram and we discuss the additional analysis employed to characterize the phase diagram. The system is described in terms of a generalized Gross-Pitaevskii theory including

the beyond-mean-field Lee-Huang-Yang correction. The energy functional is $E = E_{\mathrm{mf}} + E_{\mathrm{dd}} + E_{\mathrm{LHY}}$ with

$$E_{\mathrm{mf}} = \int \left[\frac{\hbar^2}{2m} |\nabla\psi(\boldsymbol{r})|^2 + V_{\mathrm{ho}}(\boldsymbol{r})\rho(\boldsymbol{r}) + \frac{g}{2}\rho^2(\boldsymbol{r}) \right] d\boldsymbol{r},$$

$$E_{\mathrm{dd}} = \frac{C_{\mathrm{dd}}}{2} \iint \rho(\boldsymbol{r}) V_{\mathrm{dd}}(\boldsymbol{r} - \boldsymbol{r}')\rho(\boldsymbol{r}')d\boldsymbol{r}d\boldsymbol{r}',$$

$$E_{\mathrm{LHY}} = g_{\mathrm{LHY}} \int \rho^{5/2}(\boldsymbol{r})d\boldsymbol{r}, \qquad (\mathrm{B1})$$

where $\rho(\boldsymbol{r}) = |\psi(\boldsymbol{r})|^2$ represents the condensate density, $V_{\mathrm{ho}}(\boldsymbol{r}) = (m/2)\sum_{\alpha=x,y,z} \omega_\alpha^2 r_\alpha^2$ the harmonic trapping, $g = 4\pi\hbar^2 a_s/m$ is the contact interaction strength, $V_{\mathrm{dd}}(\boldsymbol{r}) = (1 - 3\cos^2\theta)/(4\pi r^3)$ the (bare) dipole-dipole potential, $C_{\mathrm{dd}} \equiv \mu_0\mu^2$ its strength, μ the modulus of the dipole moment $\boldsymbol{\mu}$, $\boldsymbol{r}$ the distance between the dipoles, and θ the angle between the vector $\boldsymbol{r}$ and the dipole axis, $\cos\theta = \boldsymbol{\mu} \cdot \boldsymbol{r}/(\mu r)$ [48]. The orientation of the magnetic dipoles is along the z direction (the direction of the magnetic field $\boldsymbol{B}$). The LHY coefficient is $g_{\mathrm{LHY}} = [(256\sqrt{\pi})/15][(\hbar^2 a_s^{5/2})/m] \times (1 + \frac{3}{2}\epsilon_{\mathrm{dd}}^2)$, with $\epsilon_{\mathrm{dd}} = \mu_0\mu^2 N/(3g)$ [49].

The ground state of the system is obtained by minimizing the energy functional $E[\psi]$ by means of a conjugate algorithm; see, e.g., Refs. [48,50,51]. In the numerical code the double integral appearing in Eq. (B 1) is mapped into Fourier space where it can be conveniently computed by means of fast Fourier transform (FFT) algorithms, after regularization. The LHY correction in Eq. (B 1) is obtained from the expression for homogeneous 3D dipolar condensates under the local-density approximation [49,52].

To obtain the contrast in Fourier space $\tilde{C}$ from the ground-state density distributions, we first compute $|\mathcal{F}[\sqrt{\rho(x)}]|^2$, where $\rho(x)$ is the column density integrated along the transverse trap direction y. The order parameter $\tilde{C}$ is given by the height of the first lateral peak relative to the central one. A simple relation between real space C and $\tilde{C}$ can be derived in the 1D infinite case discussed in Appendix A. In the limit $C \ll 1$, we find $\tilde{C} = C^2/16$.

2. Additional data of numerical simulations

Figure 11 shows data supporting the discussion in Sec. III about the compressibility of the supersolid and the onset of the LHY-dominated regime, for the transitions at the center of the crossover. Figure 11(a) shows the transverse width σ_y normalized to that of a noninteracting system, $\ell_y/\sqrt{2}$. For $\nu_y > 70$ Hz the values are very close to 1, in agreement with the expectation that, at the transition, attractive dipolar and repulsive contact interactions tend to cancel out. Since σ_y is slightly less than $\ell_y/\sqrt{2}$, the dipolar interaction is slightly larger than the contact interaction. For smaller frequencies, instead, one notes a very rapid increase of the peak density [Fig. 11(c)].
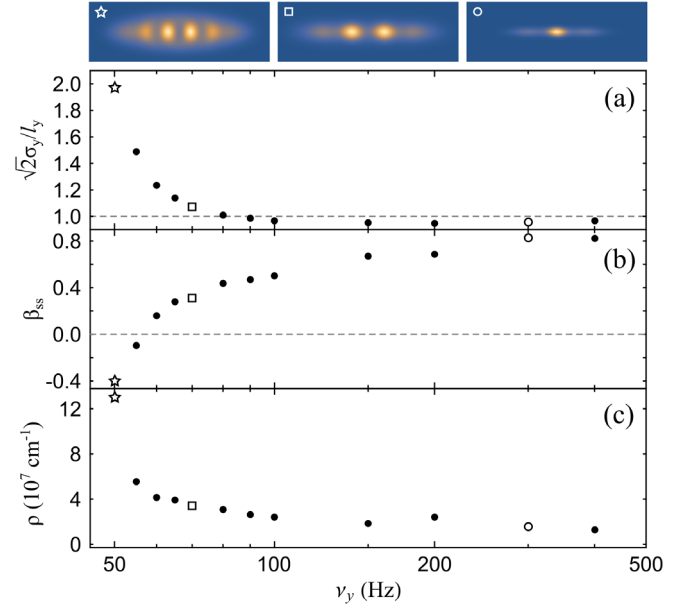

FIG. 11. Characterization of the supersolid structure for the transitions at the continuous-discontinuous boundary. (a) Transverse width σ_y, (b) deformation parameter β_{ss} of the central supersolid clusters, and (c) peak density versus transverse trap frequency. Insets: examples of the supersolid density distributions in the x-y plane.

This brings the system into a regime in which the LHY energy has an important role in limiting further density increases, due to its $\rho^{5/2}$ dependence, by increasing the transverse size of the clusters. Hence, σ_y becomes larger than the noninteracting width. In Fig. 11(b), we observe the same features in the deformation parameter $\beta_{\mathrm{ss}} = \langle x^2 - y^2 \rangle/\langle x^2 + y^2 \rangle$ of the central supersolid clusters. In an unconfined 2D system, the natural shape of the clusters in the x-y plane is circular, so that $\beta_{\mathrm{ss}} = 0$. In the trapped system studied in the main text, this happens only in a limited range of transverse trapping frequencies around $\nu_y = 60$ Hz. For larger frequencies, the clusters get squeezed by the transverse trap, so one has $\beta_{\mathrm{ss}} > 0$. For smaller frequencies, in the LHY regime, the clusters become elongated in the transverse direction and $\beta_{\mathrm{ss}} < 0$. This is the "stripe" regime found also in other numerical studies [23,39].

A different effect of the LHY energy term arises for large transverse confinements and large N, leading to a second change from continuous to discontinuous transitions, as shown in Fig. 3(a). Figure 12 shows an example of the discontinuous transition in such a regime. The characteristic features are (1) the supersolid initially forms continuously in the regions with intermediate density, where the LHY term is not too large, and not at the center as usual (a similar effect was observed numerically in Ref. [7]), (2) in a second stage, the supersolid forms also in the center, via a discontinuous transition since the LHY term there is large, (3) the discontinuous transition is accompanied by the opposite of the standard magnetostriction effect, i.e., the
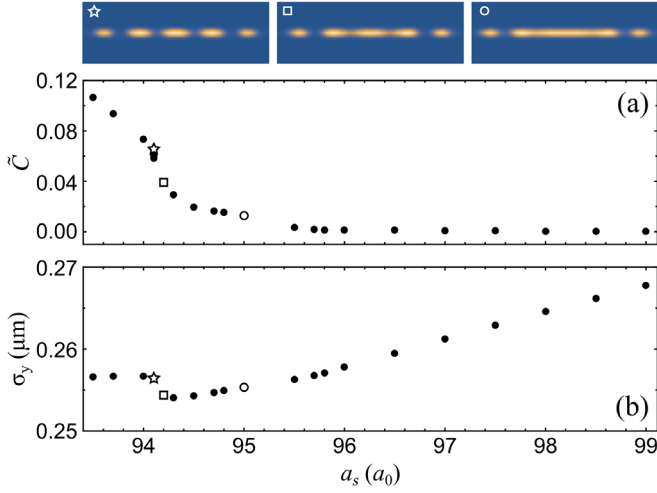
FIG. 12. Discontinuous transition in the LHY-dominated regime, ($\nu_y = 400$ Hz, $N = 7 \times 10^4$). (a) Contrast $\tilde{C}$ as a function of the scattering length. Note the initially continuous transition around $95.5a_0$, followed by a discontinuous one around $94.2a_0$. The insets show that the modulation initially forms on the sides of the distribution. (b) Behavior of σ_y across the transition, demonstrating the inverse magnetostriction provided by the LHY term.

transverse size increases when the supersolid forms, to reduce the density increase, (4) the discontinuous transition is weak, because it regards only a small fraction of the system. All these effects are a consequence of the peculiar dependence of the LHY energy term on the density $\rho^{5/2}$, which results in a stronger variation of the LHY term along the system than the contact and dipole-dipole terms.

APPENDIX C: EXPERIMENTAL METHODS AND ANALYSIS

1. Experimental sequence

The experiments start with a Bose-Einstein condensate (BEC) of about 8×10^4 ^{162}Dy atoms in a crossed optical trap. In previous experiments, we measured typical temperatures in the range 3–10 nK, through free-expansion measurements in the supersolid regime, following a discontinuous transition [5]. The condensate is initially prepared at a magnetic field $B \simeq 5.5$ G, corresponding to a scattering length of about $140a_0$. The magnetic field is then slowly changed toward the critical values for the phase transition into the supersolid, close to the set of Feshbach resonances around 5.3 G [5], with a resolution of 1 mG. The magnetic field is calibrated via radio-frequency spectroscopy before and after each experimental run, lasting typically 3–4 h. The magnetic field stability is about 0.5 mG, corresponding to a stability in scattering length of about $0.3a_0$. For the conversion from magnetic field to scattering length, we adopt the model presented in Ref. [53]. The relatively large uncertainty in the

background scattering length results in a global systematic uncertainty of several a_0 in the experimental scattering length at which the transitions take place. In all experimental figures we applied a shift to the scattering length to get a matching between the transition point identified in the experiment and that from ground-state simulations in potential V_D. We identify the experimental transition point from the jump in the atom number; see Fig. 15. The resulting shift amounts to $6.7a_0$. This analysis does not take into account the shift of the dynamical phase transition with respect to the equilibrium one, which we estimate to be of the order of $0.5a_0$; see Appendix D.

At the end of each experimental sequence, we suddenly switch off the optical potential and we let the system expand for 90 ms in the presence of a magnetic-field gradient that compensates gravity. About 200 μs before the release of the atoms we increase the contact interaction strength by setting $a_s \simeq 140a_0$ in about 1 ms, thus minimizing the relative effects of the dipolar interaction on the expansion. This helps in preserving characteristic properties such as the contrast and the period of the momentum distribution [6]. We finally measure the atomic density, which we interpret as the momentum distribution $\rho(k_x, k_y)$, by absorption imaging on the strong optical transition at 421 nm.

2. Contrast

The presence of the supersolid density modulation is revealed by the characteristic side peaks in the momentum distribution, as depicted in the insets of Fig. 6(a). To extract the contrast $\tilde{C}$, as a function both of the scattering length and of time, we analyze each image following these steps. First, we rotate the momentum distribution in the plane to align the interference peaks along the k_x direction. Second, we integrate over k_y to get the 1D momentum distribution $\rho(k_x)$. Third, we fit $\rho(k_x)$ with a double-slit model,

$$\rho(k_x) = A_0 e^{-(k_x - k_0)^2/2\sigma^2} \{1 + A_1 \sin\left[\pi(k_x - k_0)/k_r + \varphi\right]\},$$
(C1)

where A_0, k_0, and σ are, respectively, the amplitude, center, and width of the envelope, while A_1, k_r, and φ are the amplitude, period (in momentum space), and phase of the modulation. The typical experimental image has a phase of $\pi/2$ (see Fig. 14), corresponding to a central peak and two lateral, symmetric peaks. To get a contrast $\tilde{C}$ unbiased from fluctuations of the phase around $\pi/2$, we rephase the fitted function imposing $\varphi = \pi/2$ and we define $\tilde{C} = \max^L / \max^C$, where $\max^C$ and $\max^L$ are the values of the central and first lateral maxima, respectively (see Fig. 13). Since the lateral maximum in the superfluid phase does not exist, we should get $\tilde{C} = 0$ in this regime. However, trying to fit a superfluid profile with the double-slit function Eq. (C1), the fit can force the presence of small maxima in the slope of the superfluid
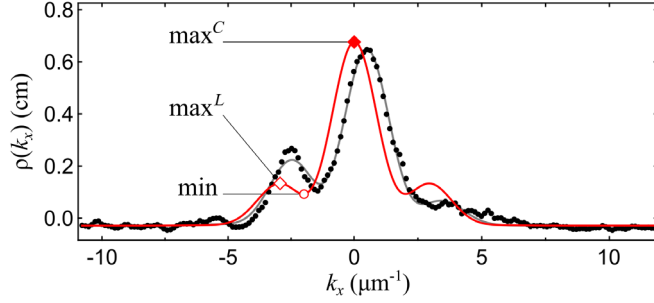
FIG. 13. Example of experimental 1D momentum distribution $\rho(k_x)$ obtained after a time-of-flight experiment in the supersolid regime of potential V_D. Black dots are experimental data, while the gray line is the fit using the double-slit function of Eq. (C1). The red line is the same fitted function after fixing the phase to $\pi/2$. The highlighted points are the central maximum $\max^C$, the lateral maximum $\max^L$, and the intermediate minimum (min) used in the definition of the observables $\tilde{C}$ and $\tilde{C}_2$ (see text).
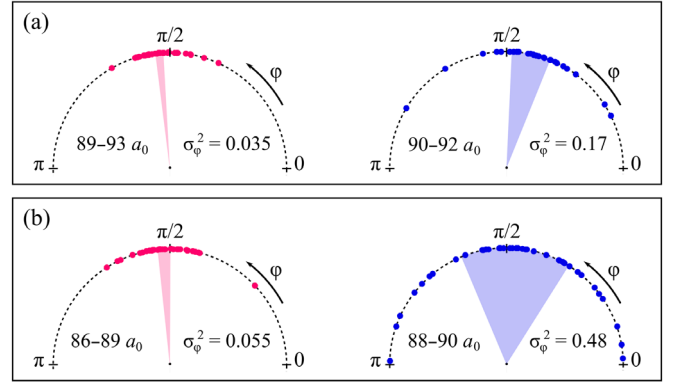

FIG. 14. Phase distributions of the interference pattern in potential V_C (magenta) and potential V_D (blue) just after the transition (a) and deeper in the supersolid regime (b). The shaded areas correspond to $\bar{\varphi} \pm \sigma_\varphi^2$, with $\bar{\varphi}$ the average phase and σ_φ^2 the variance.

and give fictitious nonzero values of $\tilde{C}$. To overcome this problem, we use a different observable defined as $\tilde{C}_2 = (\max^L - \min)/(\max^L + \min)$, where min is the first lateral minimum, and we set $\tilde{C} = 0$ if $\tilde{C}_2 = 0$. The reason is that the observable $\tilde{C}_2$ is automatically zero in the superfluid phase, since eventual fictitious lateral peaks practically coincide with their corresponding minimum. However, we do not take $\tilde{C}_2$ as a measurement of the contrast since it is very sensitive to the atom number, which is lower and lower entering the supersolid state, due to three-body losses. Typically, $\tilde{C}_2$ has a maximum lowering the scattering length and then starts decreasing. Thus, we use $\tilde{C}_2$ only to distinguish between superfluid and supersolid images.

When studying the contrast as a function of time, the fitting function is a damped sinusoid of the form

$$\tilde{C}(t) = A \sin\left(\sqrt{(2\pi\nu)^2 - \tau^2}\, t + \phi_0\right) e^{-t/\tau} + \text{off}_1 t + \text{off}_2,$$

$$(C2)$$

where ν is the frequency of the oscillation and τ the damping time. We fit with the same function also other observables which allow a direct comparison between the BEC and the supersolid, for example, the longitudinal width σ_x which features the breathing-mode oscillation [8]. From measurements performed at different values of the scattering length, see, e.g., Figs. 6(d) and 6(e), we find that the damping time decreases about an order of magnitude going from the BEC to the supersolid. For example, in the discontinuous potential V_D, we get $\tau = (100 \pm 41)$ ms at $94.3a_0$ and $\tau = (15 \pm 5)$ ms at $87.4a_0$.

3. Phase fluctuations

We verified that the measured momentum distributions $\rho(k_x)$ in the supersolid regime show phase coherence, the

property that distinguishes a supersolid from a crystal of independent droplets [5]. In Fig. 14 we plot the phase φ of the momentum distribution after crossing the transitions. For both potentials V_C and V_D we divide the data into two groups: just after the transition point, see Fig. 14(a), corresponding to the intervals $(89$–$93)a_0$ for V_C and $(90$–$92)a_0$ for V_D, and deeper into the supersolid regime, see Fig. 14(b), intervals $(86$–$89)a_0$ for V_C and $(88$–$90)a_0$ for V_D. All datasets have a variance lower than a uniform distribution, $\sigma_\varphi^2 = \pi^2/12 \simeq 0.8$, demonstrating the phase coherence of the supersolid. Interestingly, the value of the variance in the discontinuous trap is larger than in the continuous one. For potential V_D, $\sigma_\varphi^2 = 0.17$ close to the transition point, while the distribution broadens to $\sigma_\varphi^2 = 0.48$ at lower scattering lengths, in agreement with results reported in Ref. [5] where the phase transition was observed to be discontinuous. Instead, for potential V_C the phase distribution is much narrower, with $\sigma_\varphi^2 = 0.035$ and $\sigma_\varphi^2 = 0.055$ for the two datasets. This observation demonstrates that the different character of the two transitions also affects the phase excitations in the supersolid regime, other than the amplitude excitations discussed in the main text.

4. Atom number

In the experiment, the atom number tends to decrease as one moves from the superfluid into the supersolid phase, due to three-body losses, $dN/dt = -K_3\rho^2$, as depicted in Fig. 15. The losses increase mainly because ρ increases, while K_3 is approximately constant. In both cases, one reaches the supersolid regime with about 40% of the initial N. On the way back, N stays approximately constant, since the density decreased during the permanence in the supersolid regime and losses are less effective. The similar behavior of the atom number across the transitions shows that losses are similar in the two traps. The atom number in
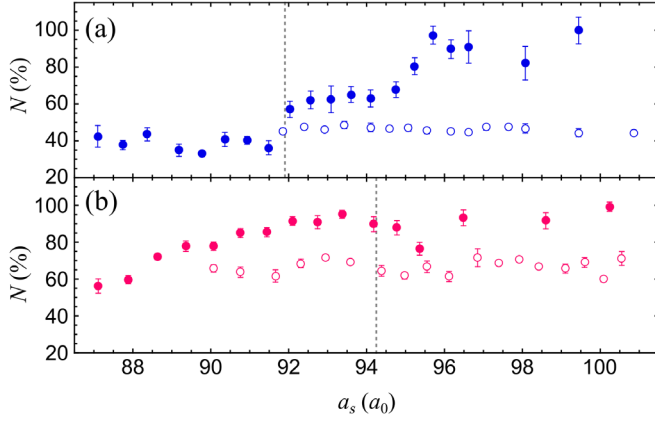
FIG. 15. Evolution of the atom number during the ingoing (filled symbols) and outgoing ramp (open symbols), respectively, for potential V_D (a) and V_C (b). Error bars are the standard deviation of the mean of 10–20 measurements. The atom number is normalized to its maximum value on the BEC side.

the supersolid quoted in the main text ($N = 3 \times 10^4$) corresponds to the measured atom number just after the transitions, with an uncertainty $\delta N = \pm 5 \times 10^3$. We checked in the simulations that in this interval of N the character of the phase transitions does not change, for both potentials.

5. Expansion energy

We use the momentum distributions $\rho(k_x, k_y)$ also to extract the expansion energy, as shown in Fig. 8. First, we compute $\delta\rho = \rho - \langle\rho\rangle$, subtracting from each distribution in the dataset the average of all the images for the corresponding harmonic potential (800 and 500 images for potentials V_D and V_C, respectively). The excess energy $E - \langle E \rangle$ is given by

$$\Delta E_{\mathrm{raw}} = \left(\frac{\hbar^2}{2m}\right) \int \delta\rho(k_x, k_y) k^2 dk_x dk_y. \quad (C3)$$

Since we use normalized momentum distributions, $\int \rho(k_x, k_y) d^2k = 1$, Eq. (C3) gives the energy per particle. In order to eliminate the effect of atom losses, the data are corrected taking into account the correlations between energy ΔE_{raw} and the atom number, given mainly by the repulsive interactions which cannot be neglected during the expansion. As shown in Fig. 16, we use a linear regression of the form $\Delta E_{\mathrm{raw}} = \gamma N + \Delta E_0$, to determine correlations in subsets with similar N, corresponding to different regions in scattering length. Raw data are then rescaled using the relation,

$$\Delta E = \Delta E_{\mathrm{raw}} - \gamma_i (N - \bar{N}), \quad (C4)$$

where $\bar{N}$ is the average atoms number in the superfluid side. In this way ΔE is increased for data with $N < \bar{N}$ and
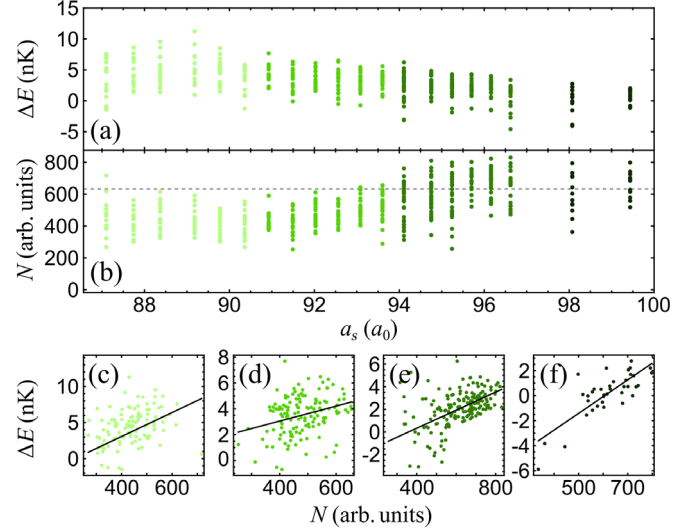

FIG. 16. Analysis of the expansion energy presented in Fig. 8. As an example we show the experimental data for the ingoing ramp in the potential V_D. Panels (a) and (b) show excess energy (raw data) and atom number as a function of the scattering length. The horizontal dashed line marks the average atom number $\bar{N}$ in the superfluid side. Different colors correspond to the subsets in (c)–(f) where the solid lines are the linear regressions used to rescale raw data in (a) using Eq. (C4).

decreased in the opposite case, by an amount proportional to γ_i for each subset. In Fig. 8, we show the mean value of data obtained from Eq. (C4).

6. Adiabaticity

To confirm the different character of the transitions in potentials V_C and V_D, we checked that the different degree of adiabaticity persists in the whole range of ramp speeds accessible in the experiment.

In a first type of experiment, we crossed twice the transition for both V_C and V_D, similarly to the main experiment shown in Fig. 6, but with a variable ramp speed. Besides the standard speed of $0.5a_0/\mathrm{ms}$ of the main experiments, we employed a speed slower by a factor of 2 and a speed faster by a factor of 2. For both V_C and V_D, the ramp starts from the superfluid side, waits 15 ms on the supersolid side, about $2a_0$ below the transition, and then ends again on the superfluid side, about $4a_0$ above the transition. To take into account excited modes of the supersolid, we averaged samples detected after waiting times of 10, 20, and 30 ms. The results are shown as open circles in Fig. 17. The contrast for V_D is always larger than the one for V_C, but both show an approximately linear increase for increasing ramp speeds. This implies that crossing twice the transition into a well-formed supersolid has a speed-dependent contribution for both continuous and discontinuous transitions. We attribute it to the finite formation time of the supersolid, about 15 ms, which is of the same order as the characteristic period of the collective
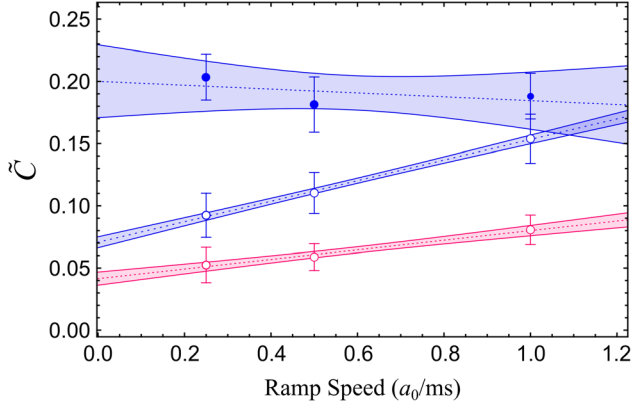
FIG. 17. Adiabaticity versus ramp speed. Contrast after a ramp from the superfluid to the onset of the supersolid (filled circles) and after crossing twice the transition (open circles), for potentials V_C (magenta) and V_D (blue). Error bars are the standard deviation of the mean. Dashed lines are linear fits and colored bands are the confidence intervals at one standard deviation.
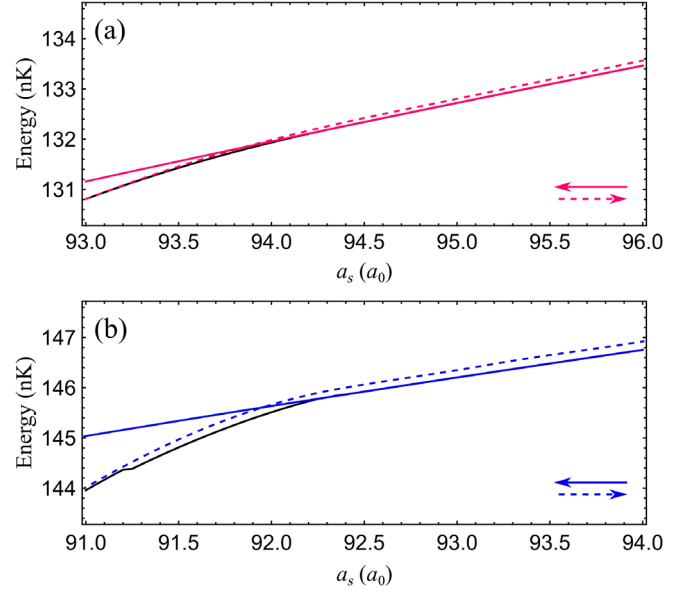

FIG. 18. Simulated energies during a slow ramp across the two phase transitions studied in the experiment. Total energy versus scattering length for the continuous (a) and discontinuous (b) cases. Different lines are associated to the ingoing ramp (solid line), the outgoing ramp (dashed line), and the ground-state energy (black line).

oscillations in the contrast. Since the ingoing ramp duration is not much longer than the formation time, the supersolid does not form with the lowest energy available.

Note that the larger final contrast for V_D than for V_C persists also extrapolating to zero ramp speed with a linear fit (dashed lines in Fig. 17). This confirms that the former transition is discontinuous. We attribute instead the zero-speed intercept for V_C to atom losses, which leads to a loss of adiabaticity in the long-time limit.

In a second type of experiment with potential V_D, we ramped the scattering length from the superfluid side into the strongly fluctuating region just prior to the stable formation of the supersolid (about $92.5a_0$). We then selected only the samples with a finite contrast, discarding those still on the superfluid side. This procedure allows us to study the supersolid just after the transition. To allow for the formation of the supersolid, we employed a minimum waiting time of 15 ms. Also in this case we averaged samples detected after waiting times of 10, 20, and 30 ms. The mean value of the contrast for varying ramp speed is shown in Fig. 17 as filled circles. One notes that the mean contrast stays approximately constant, confirming the discontinuous character of the phase transition.

APPENDIX D: NUMERICAL SIMULATIONS OF THE DYNAMICS

We simulated the evolution of the system when crossing the phase transitions in potentials V_C and V_D by solving the Gross-Pitaevskii equation $i\hbar\partial_t\psi = \delta E/\delta\psi^*$, by using the FFT split-step method discussed in Ref. [54]. The typical size of the numerical box is $24\ \mu m$ per side, each discretized in 128 points.

We found that the speed of the ramp in scattering length employed in the experiment, $0.5a_0/ms$, in the simulations

produces effects more similar to a sudden quench of the scattering length than to an adiabatic transformation. This is presumably due to the lack of dissipation in the simulations. A ramp slower by one order of magnitude, $0.06a_0/ms$, results instead in a quasiadiabatic crossing of the phase transition in potential V_C, see Fig. 18, similarly to the experiment. For such a ramp speed, the simulations for the potential V_D show an increase of energy of about 1 nK, which is of the same order of magnitude of the experimental observation. A quantitative comparison of the energies in the experiment and in the simulations is not possible, mainly because of the increased contact energy in the expansion phase of the experiment. Note indeed that while the simulated energy decreases while lowering a_s, mainly because of the decrease of contact energy, the experimental energy in Fig. 8 increases, because higher densities enhance the effect of the repulsive contact interaction during the expansion.

Samples of the dynamics for V_C are shown in Fig. 7 and discussed in the main text. The simulations for potential V_D feature a similar behavior, i.e., excitation of collective modes of the supersolid and of the superfluid for the ingoing and outgoing ramps, respectively. The number of modes is, however, larger than for potential V_C, in agreement with both the larger number of modes observed in the experiment and the larger excitation energy of Fig. 18. In general, the simulations feature a larger number of modes than the experiment, presumably because they lack the dissipation that is instead present in the experiment.

We also studied the hysteresis for the discontinuous transition in potential V_D, in the hypothetical scenario in which the transition is crossed in both directions starting from the ground state of the system. The amplitude of the hysteresis cycle is about $0.5a_0$, for a holding time $t_{\text{hold}} = 40$ ms. Previous simulations for a configuration close to that of potential V_D found a similar result [6]. The hysteresis tends to disappear if one instead crosses the transition twice from the superfluid side, remaining on an excited state of the supersolid, similarly to the experimental scenario.

In conclusion, although the present simulations cannot reproduce quantitatively the observations, possibly because they do not account for temperature and dissipation effects, they support the experimental observation of a different behavior of the amplitude mode and of the energy for the continuous and discontinuous transitions, as well as the excitation of a collective mode of the superfluid following the outgoing ramp.

---

[1] E. P. Gross, *Unified Teory of Interacting Bosons*, Phys. Rev. **106**, 161 (1957).

[2] A. F. Andreev and I. M. Lifshitz, *Quantum Theory of Defects in Crystals*, Sov. Phys. Usp. **13**, 670 (1971).

[3] G. V. Chester, *Speculations on Bose-Einstein Condensation and Quantum Crystals*, Phys. Rev. A **2**, 256 (1970).

[4] A. J. Leggett, *Can a Solid be "Superfluid"?*, Phys. Rev. Lett. **25**, 1543 (1970).

[5] L. Tanzi, E. Lucioni, F. Famà, J. Catani, A. Fioretti, C. Gabbanini, R. N. Bisset, L. Santos, and G. Modugno, *Observation of a Dipolar Quantum Gas with Metastable Supersolid Properties*, Phys. Rev. Lett. **122**, 130405 (2019).

[6] F. Böttcher, J.-N. Schmidt, M. Wenzel, J. Hertkorn, M. Guo, T. Langen, and T. Pfau, *Transient Supersolid Properties in an Array of Dipolar Quantum Droplets*, Phys. Rev. X **9**, 011051 (2019).

[7] L. Chomaz, D. Petter, P. Ilzhöfer, G. Natale, A. Trautmann, C. Politi, G. Durastante, R. M. W. van Bijnen, A. Patscheider, M. Sohmen, M. J. Mark, and F. Ferlaino, *Long-Lived and Transient Supersolid Behaviors in Dipolar Quantum Gases*, Phys. Rev. X **9**, 021012 (2019).

[8] L. Tanzi, S. M. Roccuzzo, E. Lucioni, F. Famà, A. Fioretti, C. Gabbanini, G. Modugno, A. Recati, and S. Stringari, *Supersolid Symmetry Breaking from Compressional Oscillations in a Dipolar Quantum Gas*, Nature (London) **574**, 382 (2019).

[9] M. Guo, F. Böttcher, J. Hertkorn, J.-N. Schmidt, M. Wenzel, H. P. Büchler, T. Langen, and T. Pfau, *The Low-Energy Goldstone Mode in a Trapped Dipolar Supersolid*, Nature (London) **574**, 386 (2019).

[10] G. Natale, R. M. W. van Bijnen, A. Patscheider, D. Petter, M. J. Mark, L. Chomaz, and F. Ferlaino, *Excitation Spectrum of a Trapped Dipolar Supersolid and Its Experimental Evidence*, Phys. Rev. Lett. **123**, 050402 (2019).

[11] L. Tanzi, J. G. Maloberti, G. Biagioni, A. Fioretti, C. Gabbanini, and G. Modugno, *Evidence of Superfluidity in a Dipolar Supersolid from Nonclassical Rotational Inertia*, Science **371**, 1162 (2021).

[12] M. A. Norcia, C. Politi, L. Klaus, E. Poli, M. Sohmen, M. J. Mark, R. N. Bisset, L. Santos, and F. Ferlaino, *Two-Dimensional Supersolidity in a Dipolar Quantum Gas*, Nature (London) **596**, 357 (2021).

[13] J. Léonard, A. Morales, P. Zupancic, T. Esslinger, and T. Donner, *Supersolid Formation in a Quantum Gas Breaking a Continuous Translational Symmetry*, Nature (London) **543**, 87 (2017).

[14] J.-R. Li, J. Lee, W. Huang, S. Burchesky, B. Shteynas, F. Ç. Top, A. O. Jamison, and W. Ketterle, *A Stripe Phase with Supersolid Properties in Spin–Orbit-Coupled Bose–Einstein Condensates*, Nature (London) **543**, 91 (2017).

[15] J. Hertkorn, J.-N. Schmidt, F. Böttcher, M. Guo, M. Schmidt, K. S. H. Ng, S. D. Graham, H. P. Büchler, T. Langen, M. Zwierlein, and T. Pfau, *Density Fluctuations across the Superfluid-Supersolid Phase Transition in a Dipolar Quantum Gas*, Phys. Rev. X **11**, 011037 (2021).

[16] M. Sohmen, C. Politi, L. Klaus, L. Chomaz, M. J. Mark, M. A. Norcia, and F. Ferlaino, *Birth, Life, and Death of a Dipolar Supersolid*, Phys. Rev. Lett. **126**, 233401 (2021).

[17] Y. Pomeau and S. Rica, *Dynamics of a Model of Supersolid*, Phys. Rev. Lett. **72**, 2426 (1994).

[18] T. Macrì, F. Maucher, F. Cinti, and T. Pohl, *Elementary Excitations of Ultracold Soft-Core Bosons across the Superfluid-Supersolid Phase Transition*, Phys. Rev. A **87**, 061602(R) (2013).

[19] Z.-K. Lu, Y. Li, D. S. Petrov, and G. V. Shlyapnikov, *Stable Dilute Supersolid of Two-Dimensional Dipolar Bosons*, Phys. Rev. Lett. **115**, 075303 (2015).

[20] N. Sepúlveda, C. Josserand, and S. Rica, *Nonclassical Rotational Inertia Fraction in a One-Dimensional Model of a Supersolid*, Phys. Rev. B **77**, 054513 (2008).

[21] J. Léonard, A. Morales, P. Zupancic, T. Donner, and T. Esslinger, *Monitoring and Manipulating Higgs and Gold-stone Modes in a Supersolid Quantum Gas*, Science **358**, 1415 (2017).

[22] Y.-C. Zhang, F. Maucher, and T. Pohl, *Supersolidity around a Critical Point in Dipolar Bose-Einstein Condensates*, Phys. Rev. Lett. **123**, 015301 (2019).

[23] Y.-C. Zhang, T. Pohl, and F. Maucher, *Phases of Supersolids in Confined Dipolar Bose-Einstein Condensates*, Phys. Rev. A **104**, 013310 (2021).

[24] S. M. Roccuzzo and F. Ancilotto, *Supersolid Behavior of a Dipolar Bose-Einstein Condensate Confined in a Tube*, Phys. Rev. A **99**, 041601(R) (2019).

[25] P. B. Blakie, D. Baillie, L. Chomaz, and F. Ferlaino, *Supersolidity in an Elongated Dipolar Condensate*, Phys. Rev. Research **2**, 043318 (2020).

[26] D. Petter, A. Patscheider, G. Natale, M. J. Mark, M. A. Baranov, R. van Bijnen, S. M. Roccuzzo, A. Recati, B. Blakie, D. Baillie, L. Chomaz, and F. Ferlaino, *Bragg Scattering of an Ultracold Dipolar Gas across the Phase Transition from Bose-Einstein Condensate to Supersolid in the Free-Particle Regime*, Phys. Rev. A **104**, L011302 (2021).

[27] J. Hertkorn, J.-N. Schmidt, M. Guo, F. Böttcher, K. S. H. Ng, S. D. Graham, P. Uerlings, H. P. Büchler, T. Langen, M. Zwierlein, and T. Pfau, *Supersolidity in Two-Dimensional*

Trapped Dipolar Droplet Arrays, Phys. Rev. Lett. **127**, 155301 (2021).

[28] T. Bland, E. Poli, C. Politi, L. Klaus, M. A. Norcia, F. Ferlaino, L. Santos, and R. N. Bisset, *Two-Dimensional Supersolidity in a Circular Trap*, arXiv:2107.06680.

[29] P. M. Chaikin and T. C. Lubensky, *Principles of Condensed Matter Physics* (Cambridge University Press, Cambridge, England, 1995).

[30] R. E. Rosensweig, *Ferrohydrodynamics* (Dover Publications, Mineola, NY, 2013).

[31] L. V. Levitin, B. Yager, L. Sumner, B. Cowan, A. J. Casey, J. Saunders, N. Zhelev, R. G. Bennett, and J. M. Parpia, *Evidence for a Spatially Modulated Superfluid Phase of* ^{3}He *under Confinement*, Phys. Rev. Lett. **122**, 085301 (2019).

[32] A. J. Shook, V. Vadakkumbatt, P. S. Yapa, C. Doolin, R. Boyack, P. H. Kim, G. G. Popowich, F. Souris, H. Christani, J. Maciejko, and J. P. Davis, *Stabilized Pair Density Wave via Nanoscale Confinement of Superfluid* ^{3}He, Phys. Rev. Lett. **124**, 015301 (2020).

[33] D. F. Agterberg, J. S. Davis, S. D. Edkins, E. Fradkin, D. J. Van Harlingen, S. A. Kivelson, P. A. Lee, L. Radzihovsky, J. M. Tranquada, and Y. Wang, *The Physics of Pair-Density Waves: Cuprate Superconductors and Beyond*, Annu. Rev. Condens. Matter Phys. **11**, 231 (2020).

[34] A. R. P. Lima and A. Pelster, *Beyond Mean-Field Low-Lying Excitations of Dipolar Bose Gases*, Phys. Rev. A **86**, 063609 (2012).

[35] L. Santos, G. V. Shlyapnikov, and M. Lewenstein, *Roton-Maxon Spectrum and Stability of Trapped Dipolar Bose-Einstein Condensates*, Phys. Rev. Lett. **90**, 250403 (2003).

[36] L. Chomaz, R. M. W. van Bijnen, D. Petter, G. Faraoni, S. Baier, J. H. Becher, M. J. Mark, F. Wächtler, L. Santos, and F. Ferlaino, *Observation of Roton Mode Population in a Dipolar Quantum Gas*, Nat. Phys. **14**, 442 (2018).

[37] B. I. Halperin, T. C. Lubensky, and S.-k. Ma, *First-Order Phase Transitions in Superconductors and Smectic-a Liquid Crystals*, Phys. Rev. Lett. **32**, 292 (1974).

[38] K. Huang, *Statistical Mechanics* (John Wiley & Sons, New York, 1987).

[39] J. Hertkorn, J.-N. Schmidt, M. Guo, F. Böttcher, K. S. H. Ng, S. D. Graham, P. Uerlings, T. Langen, M. Zwierlein, and T. Pfau, *Pattern Formation in Quantum Ferrofluids: From Supersolids to Superglasses*, Phys. Rev. Research **3**, 033125 (2021).

[40] R. M. Wilson, S. Ronen, J. L. Bohn, and H. Pu, *Manifestations of the Roton Mode in Dipolar Bose-Einstein Condensates*, Phys. Rev. Lett. **100**, 245302 (2008).

[41] D. Petter, G. Natale, R. M. W. van Bijnen, A. Patscheider, M. J. Mark, L. Chomaz, and F. Ferlaino, *Probing the Roton Excitation Spectrum of a Stable Dipolar Bose Gas*, Phys. Rev. Lett. **122**, 183401 (2019).

[42] L. Bonnes and S. Wessel, *Generic First-Order versus Continuous Quantum Nucleation of Supersolidity*, Phys. Rev. B **84**, 054510 (2011).

[43] Y. Imry, *Finite-Size Rounding of a First-Order Phase Transition*, Phys. Rev. B **21**, 2042 (1980).

[44] M. N. Tengstrand, D. Boholm, R. Sachdeva, J. Bengtsson, and S. M. Reimann, *Persistent Currents in Toroidal Dipolar Supersolids*, Phys. Rev. A **103**, 013313 (2021).

[45] S. M. Roccuzzo, S. Stringari, and A. Recati, *Supersolid Edge and Bulk Phases of a Dipolar Quantum Gas in a Box*, Phys. Rev. Research **4**, 013086 (2022).

[46] X.-Y. Luo, Y.-Q. Zou, L.-N. Wu, Q. Liu, M.-F. Han, M. K. Tey, and L. You, *Deterministic Entanglement Generation from Driving through Quantum Phase Transitions*, Science **355**, 620 (2017).

[47] L. Pezzè, A. Smerzi, M. K. Oberthaler, R. Schmied, and P. Treutlein, *Quantum Metrology with Nonclassical States of Atomic Ensembles*, Rev. Mod. Phys. **90**, 035005 (2018).

[48] S. Ronen, D. C. E. Bortolotti, and J. L. Bohn, *Bogoliubov Modes of a Dipolar Condensate in a Cylindrical Trap*, Phys. Rev. A **74**, 013623 (2006).

[49] F. Wächtler and L. Santos, *Ground-State Properties and Elementary Excitations of Quantum Droplets in Dipolar Bose-Einstein Condensates*, Phys. Rev. A **94**, 043618 (2016).

[50] W. H. Press, S. A. Teukolsky, W. T. Vetterling, and B. P. Flannery, *Numerical Recipes: The Art of Scientific Computing*, 3rd ed. (Cambridge University Press, New York, 2007).

[51] M. Modugno, L. Pricoupenko, and Y. Castin, *Bose-Einstein Condensates with a Bent Vortex in Rotating Traps*, Eur. Phys. J. D **22**, 235 (2003).

[52] M. Schmitt, M. Wenzel, F. Böttcher, I. Ferrier-Barbut, and T. Pfau, *Self-Bound Droplets of a Dilute Magnetic Quantum Liquid*, Nature (London) **539**, 259 (2016).

[53] F. Böttcher, M. Wenzel, J.-N. Schmidt, M. Guo, T. Langen, I. Ferrier-Barbut, T. Pfau, R. Bombín, J. Sánchez-Baena, J. Boronat, and F. Mazzanti, *Dipolar Quantum Droplets beyond the Extended Gross-Pitaevskii Equation*, Phys. Rev. Research **1**, 033088 (2019).

[54] B. Jackson, J. F. McCann, and C. S. Adams, *Output Coupling and Flow of a Dilute Bose-Einstein Condensate*, J. Phys. B **31**, 4489 (1998).